Supplementary Material for

Reversible subsidence on the North West Shelf of Australia

Michael Gurnis[1], Michelle Kominz[2], and Stephen J. Gallagher[3]

1. Seismological Laboratory, California Institute of Technology, Pasadena, CA 91125, USA
2. Department of Geological and Environmental Sciences, Western Michigan University, Kalamazoo, MI 49008, USA
3. School of Earth Sciences, The University of Melbourne, Melbourne, VIC 3010, Australia

Oct. 31, 2019

Site	Industry Well	Depth at Base	Age at Base	Approx. Age at Base
U1459	Houtman-1[1]	3683 m	Bajocian	170 Ma
U1460	Marangie-1[2]	3641 m	Capitanian	265 Ma
U1461	West Tryal Rocks-2[3]	3641 m	Carnian	236 Ma
U1462	Fisher[4] (new age/WD)	3345 m (964-1221)	Norian	209 Ma
U1463	Picard[5]	4145 m	Hettangian	200 Ma
U1464	no well	3000 m		

Table S1. Industry wells used to estimate compaction beneath the IODP sites. References: 1. Galloway (1978); (Smith and Sandwell, 1997); 2. Burt (2003); 3. Young and Wright (1975); 4. Woodside (1982); 5. BOC (1972).

Additional Information on Well Completion Reports

Esso Australia, 1978. Houtman-1; Well Completion Report; Basic & Interpretative Data
Origin Energy, 2004. Morangie-1/ST1; Well Completion Report; Basic & Interpretative Data
WAPET, 1975. West Tryal Rocks-2; Well Completion Report; Basic & Interpretative Data
Woodside Energy, 1972. Picard-1; Well Completion Report; Basic & Interpretative Data
Woodside Energy, 1982. Fisher-1; Well Completion Report; Basic & Interpretative Data

The well completion reports above can be downloaded from this site:
https://wapims.dmp.wa.gov.au/WAPIMS/Search/Wells

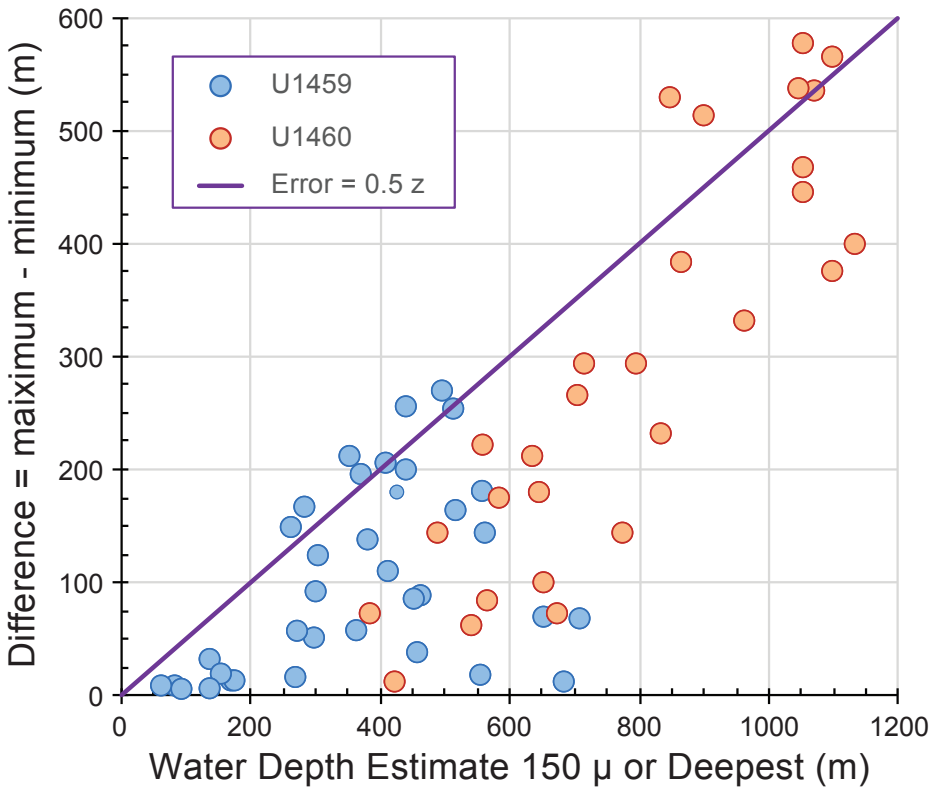

Fig. S1. Fig. S1. Estimated minimum and maximum water depths at IODP sites U1459 and U1450 in the Perth Basin (Buckley, 2016) by analysis of microfossils in two size fractions. In this plot the average water depth is plotted vs. the water depth range for all analyses. Most data points plot below the indicated line, Error Range = 0.5*Water Depth. By using this relationship to estimate water depth uncertainty at the remaining IODP sites, our error bars are generally greater than or equal to the uncertainty associated with this method.

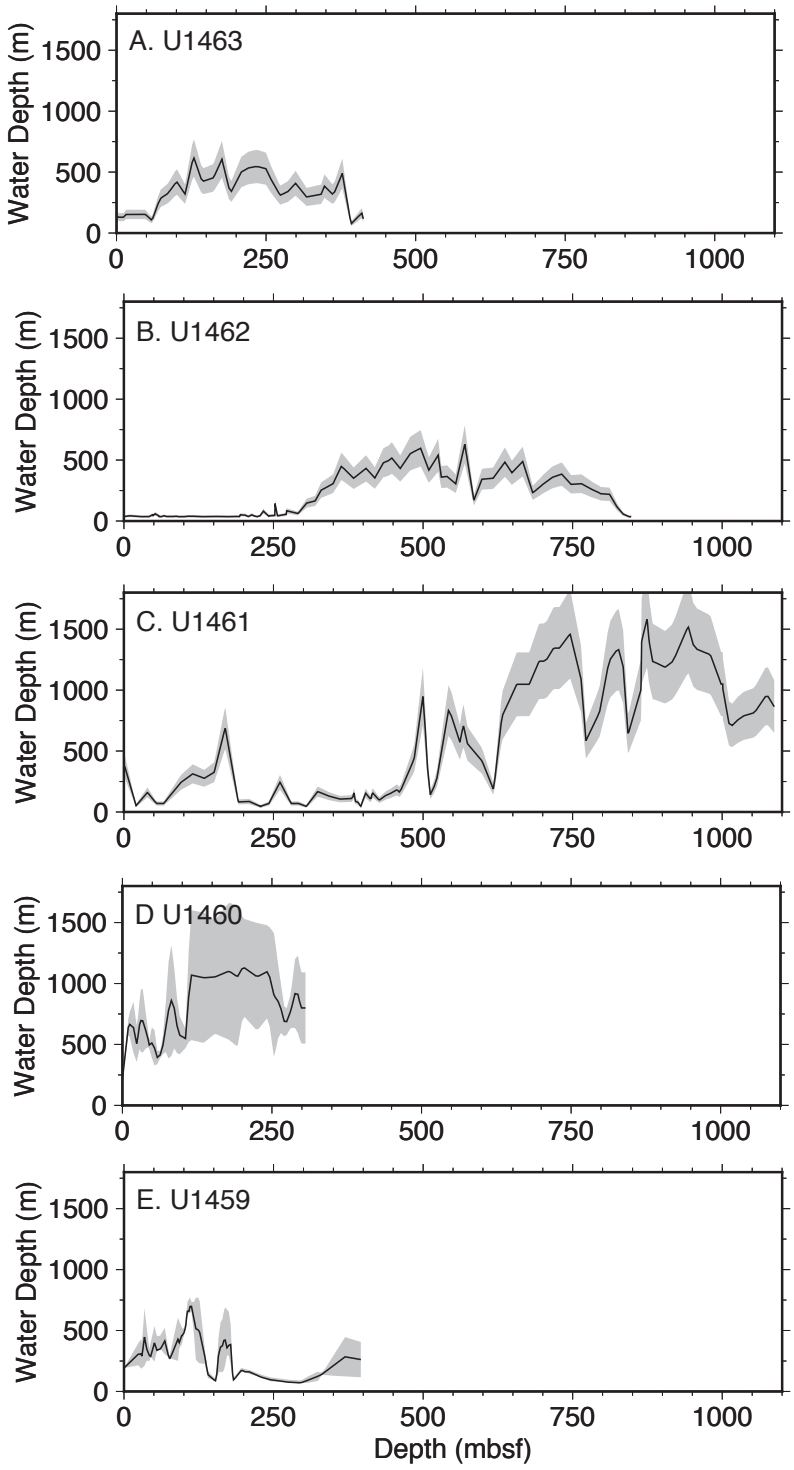

Figure S2. Water depths for U1459, U1460, U1461, U1462 and U1463. See Fig. S1 for information on how the indicated error was computed.

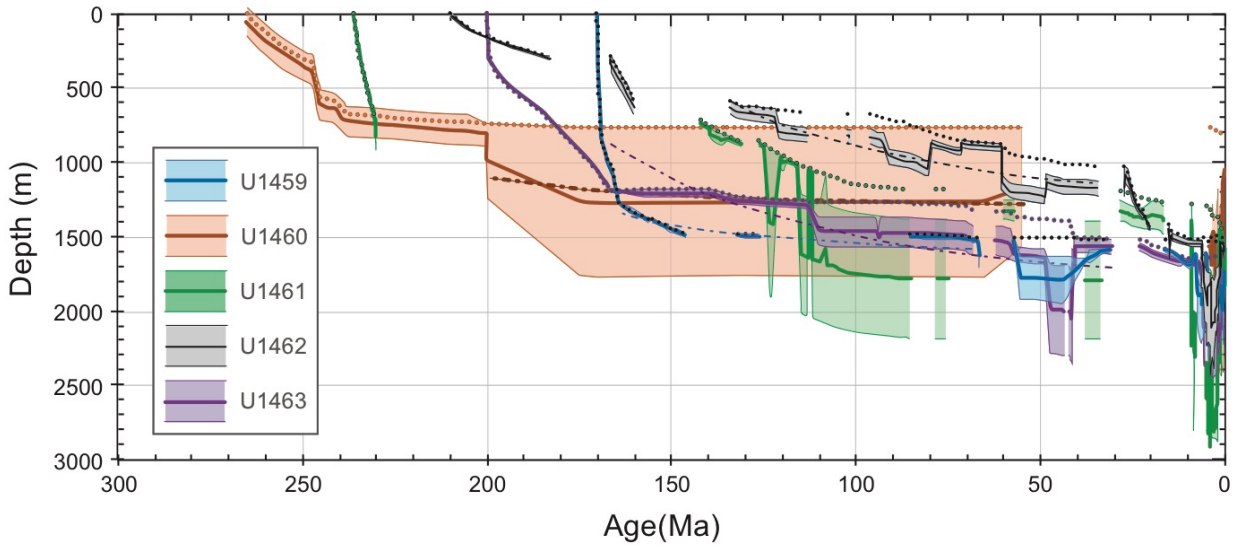

Fig. S3. Tectonic subsidence analysis of coupled industry and IODP cores. The complex and long-term nature of tectonic subsidence of the NWS is clear from the 5 wells shown. There is clearly rapid and significant departure in the last 10 million years (as detailed in Fig. 1). The curves are identified by the overlying IODP site. Industry wells (see also Table S1) are: U1459 is underlain by the Hautman-1 well; U1460 is underlain by the Morangie-1 well; U1461 is underlain by the West Tryal Rocks-2 well; U1462 is underlain by the Fisher-1 well and U1463 is underlain by the Picard-1 well. For each well, the thick line indicates tectonic subsidence based on best-estimate of water depths. The range of water-depth uncertainty is given by the shaded region and the tectonic subsidence based on sediment thicknesses alone are shown by the dotted lines.

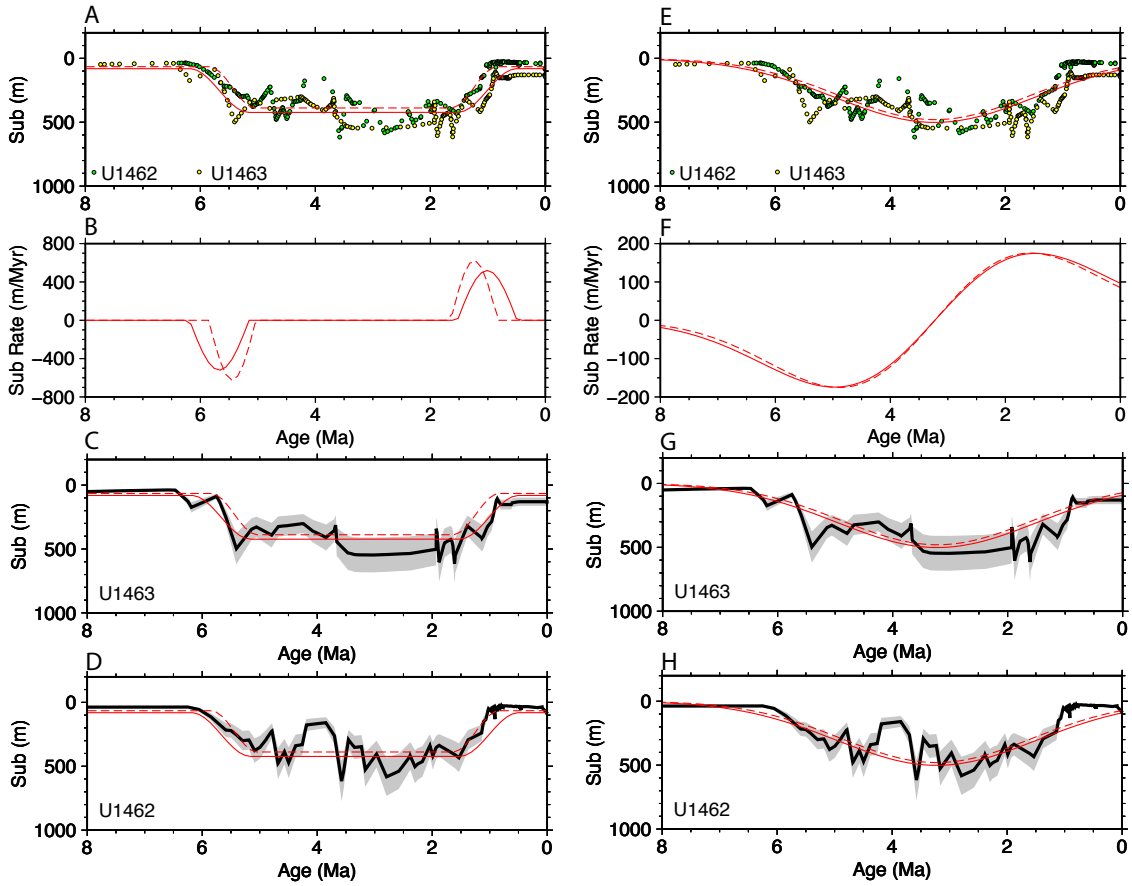

Figure S4. Least squares analysis of U1462 and U1463 tectonic subsidence with different functional forms, a harmonic composite (as described in the text) on the left and a Gaussian on the right. A & E. Tectonic subsidence values shifted so that present value equals present water depth. The solid and dashed curves are the fits with the largest and smallest amplitudes B & F. Slopes of the fits shown in A & E. C & D. The two fits compared to U1463. D & H. The two fits compared to U1462. Note that the Gaussian curves on the right significant underestimate the slops of the subsidence and uplift phases.

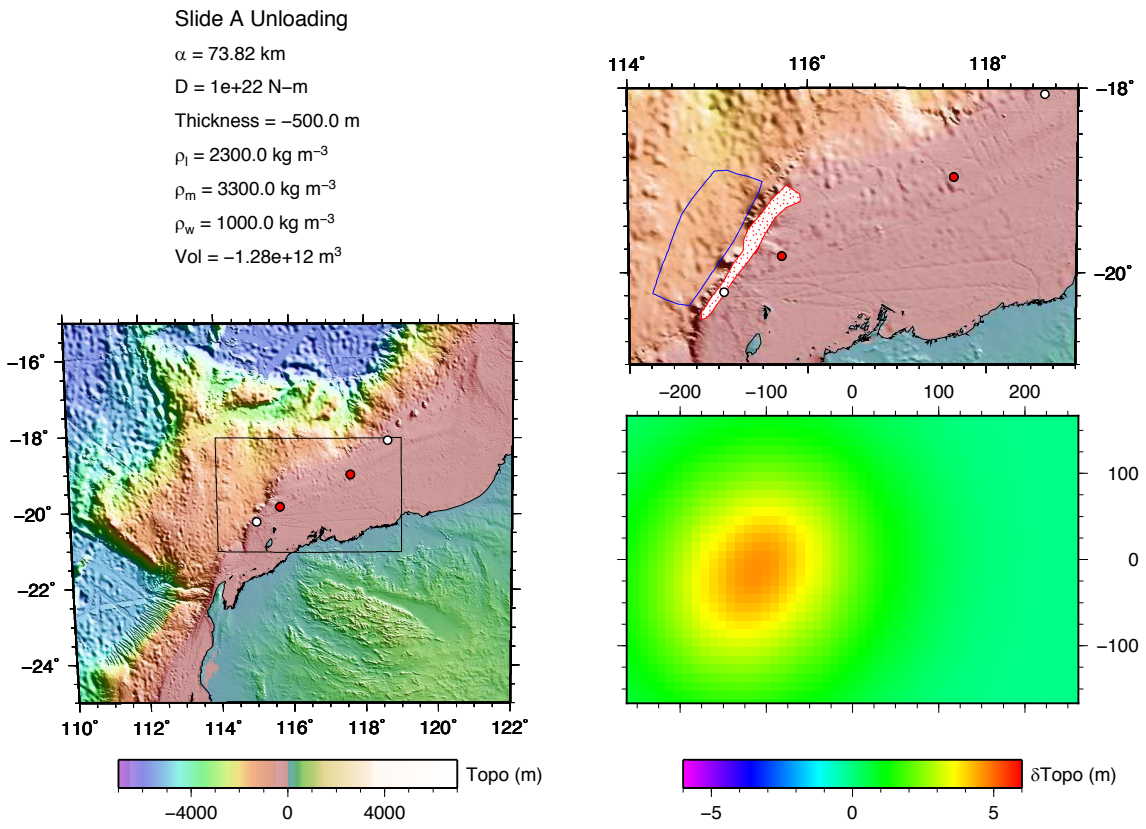

Figure S5. Predicted vertical motions associated with the unloading of slide Model A (Table 2) as described in the text. The area covered by source of slide Model A is shown in the upper right as the area stippled with red dots. The vertical motion is shown in the lower right using the elastic plate parameters tabulated in the upper left.

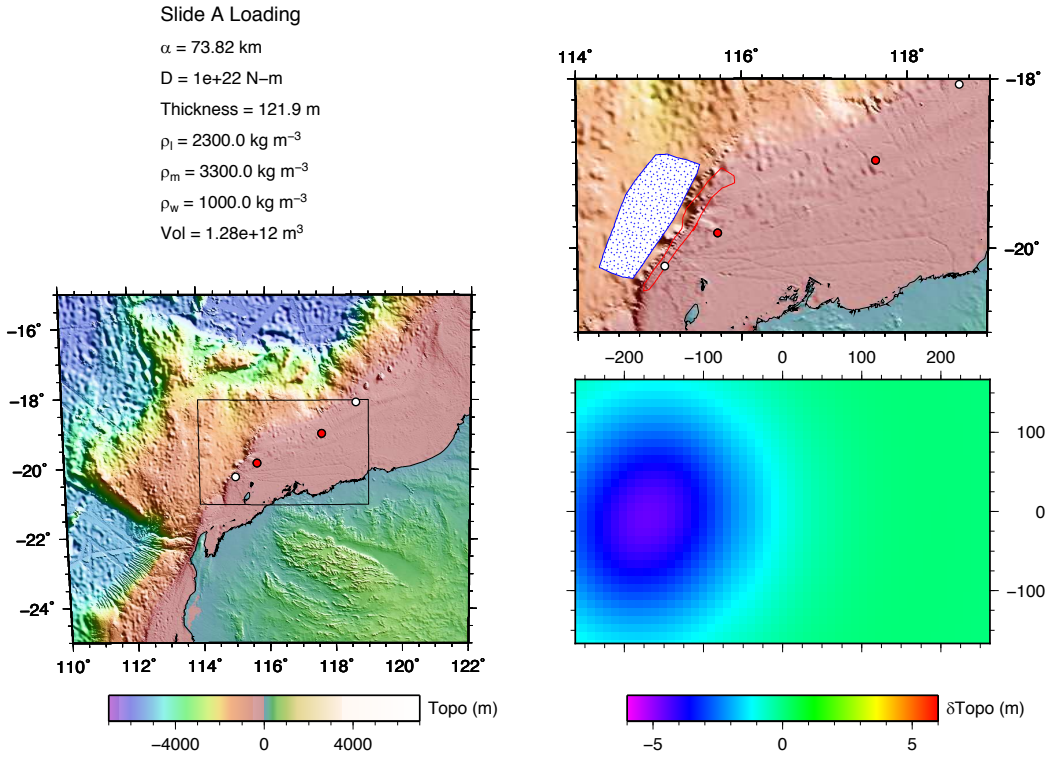

Figure S6. Predicted vertical motions associated with the loading of slide Model A (Table 2) as described in the text. The area covered by the outflow of slide Model A is shown in the upper right as the area stippled with blue dots. The vertical motion is shown in the lower right using the elastic plate parameters tabulated in the upper left.

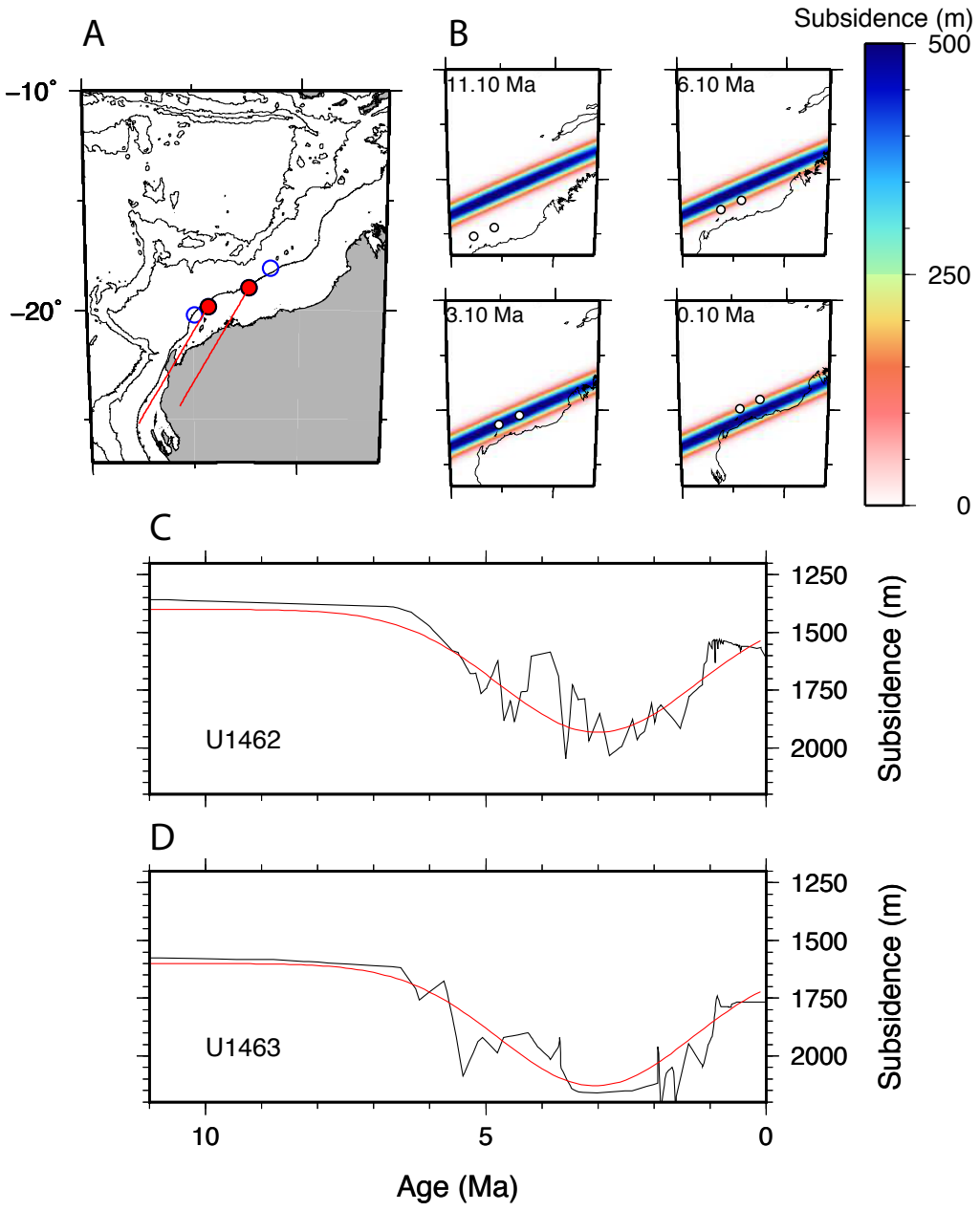

Figure S7. Predictions of simple anomaly fixed to the mantle. A. Position of drill sites with plate motions with respect to the mantle since 11 Ma (red lines) using rotations from Seton et al. (2012). B. Motion of coastline and drill sites in mantle frame with fixed ellipsoidal dynamic topography low with covariance in minor direction being 2,000 km^2. Changing dynamic topography at Sites U1462 (C) and U1463 (D) in red compared against tectonic subsidence (black).

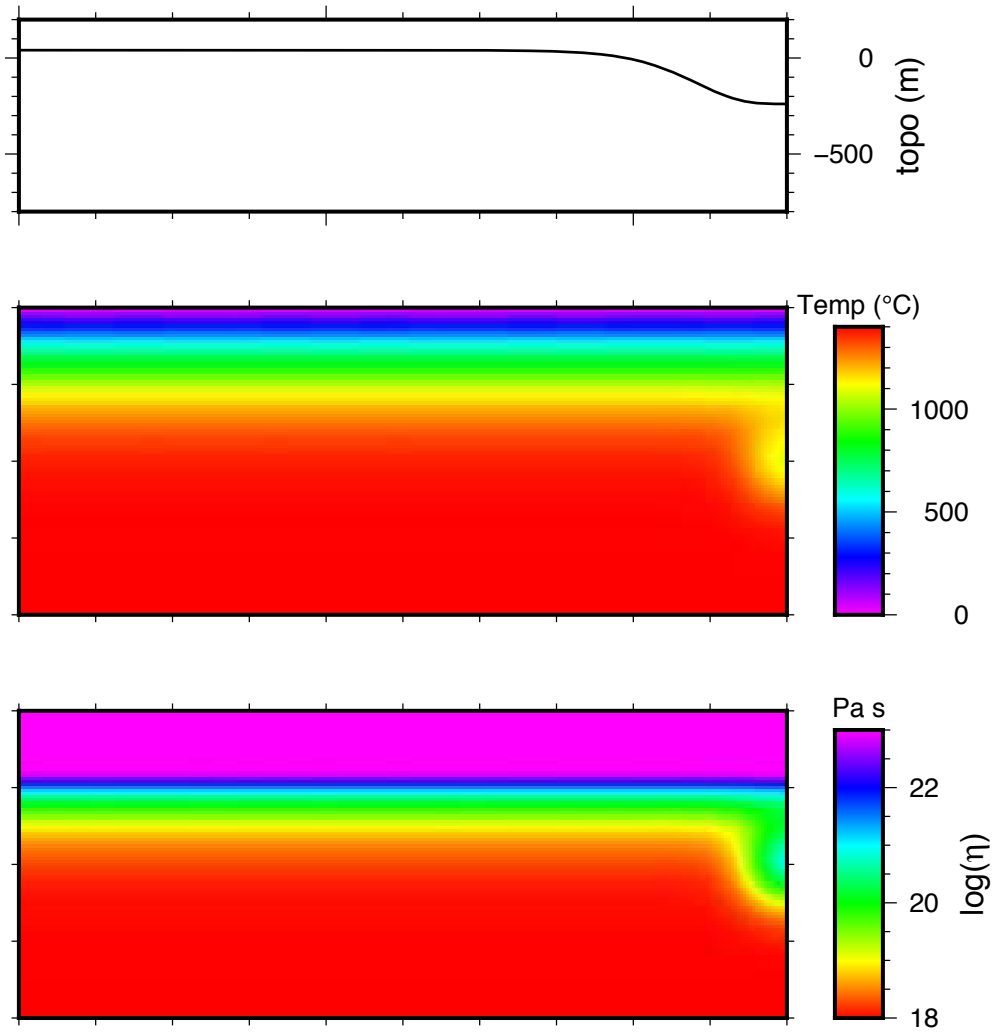

Figure S8. Set up and prediction of mantle flow model (model Sink01) in which the anomaly is detached from the lithosphere (See computational details below). Top panel is the predicted dynamic topography, the middle panel the scaled temperature, and the bottom panel the scaled dynamic viscosity. The scaled depth of the box is 400 km and the scaled width 1,000 km. See Tables S2 and S4 for model and scaling parameters.

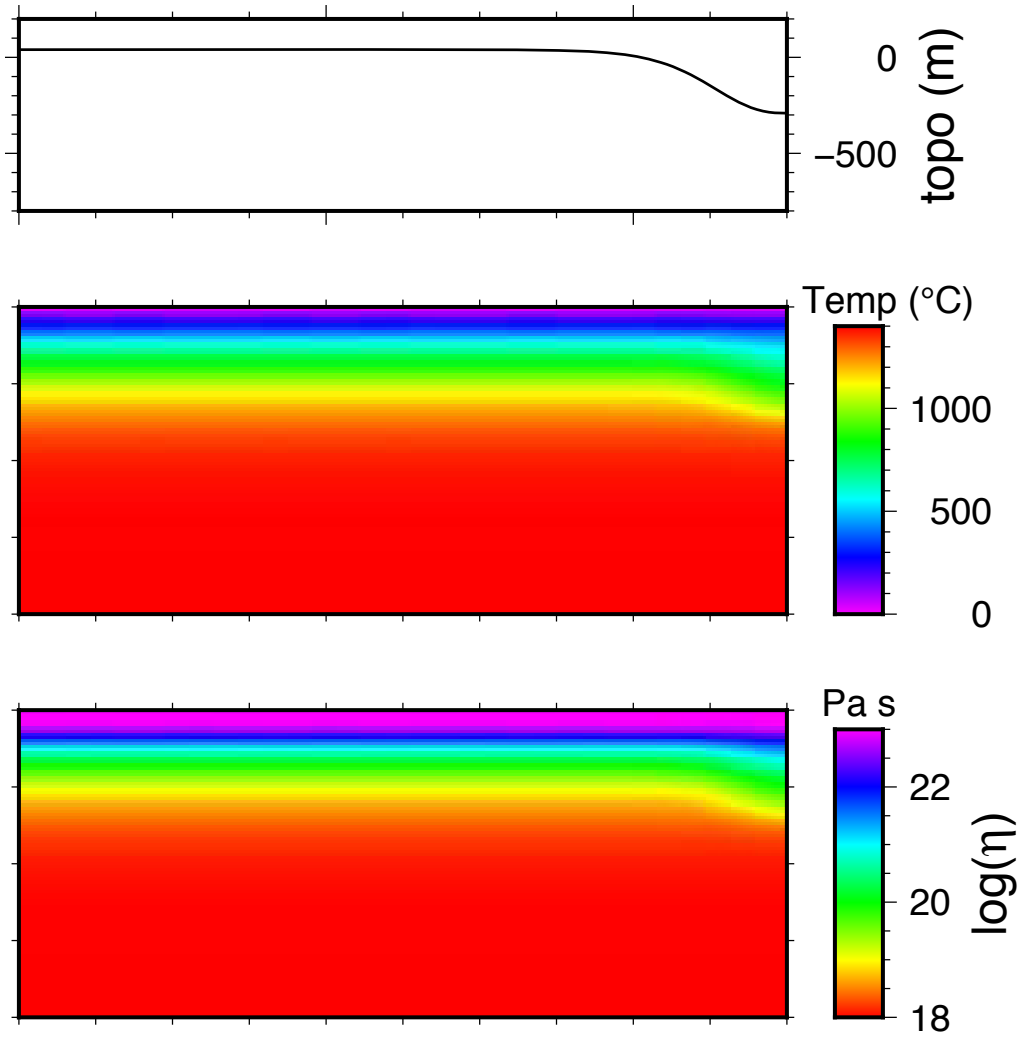

Figure S9. Set up and prediction of mantle flow model (model AL01) in which the anomaly is attached to the lithosphere (See computational details below). Top panel is the predicted dynamic topography, the middle panel the scaled temperature, and the bottom panel the scaled dynamic viscosity. The scaled depth of the box is 400 km and the scaled width 1,000 km. See Tables S2 and S3 for model and scaling parameters.

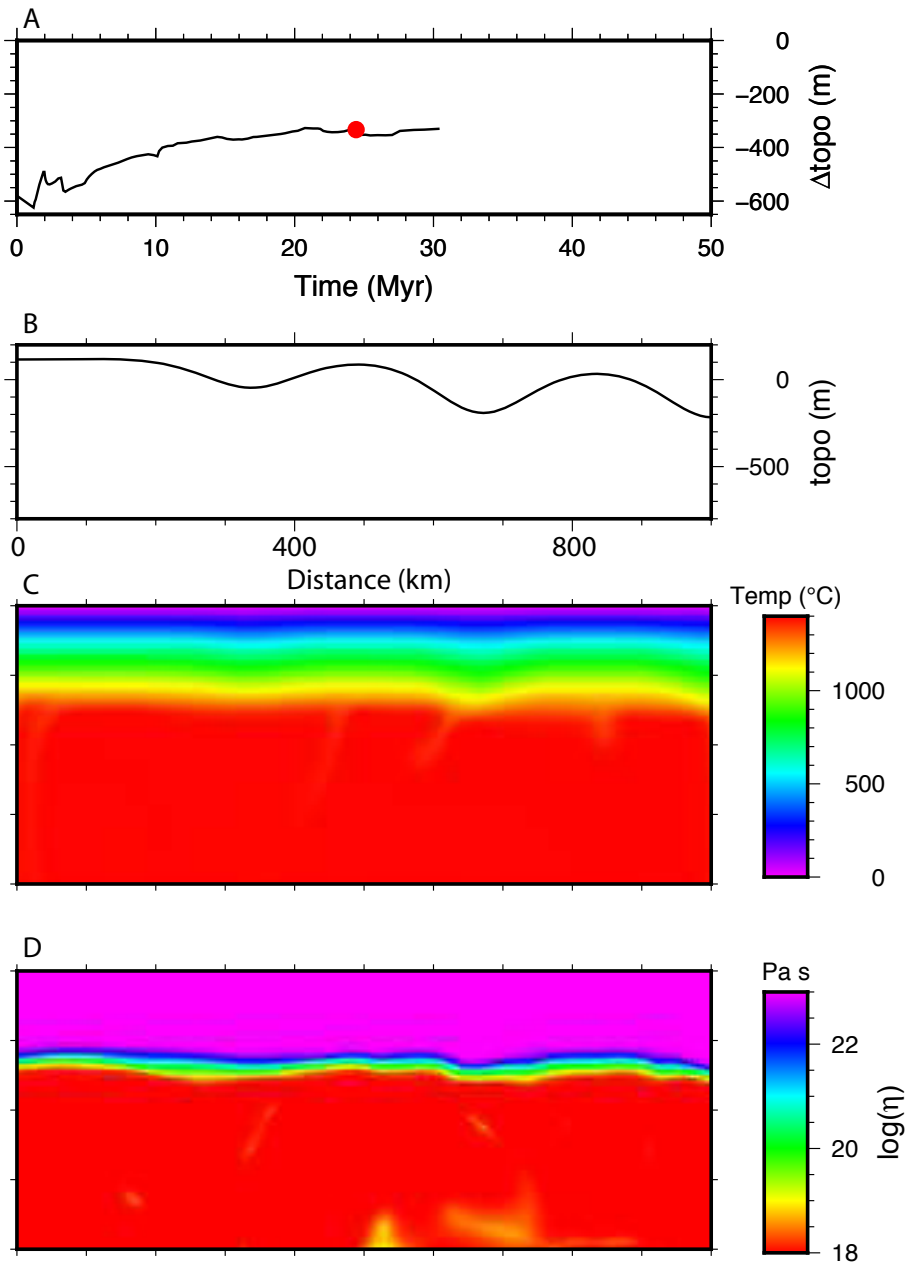

Figure S10. Small scale convection model (Model SSC14 indicated in Figure 7 of the main text and in Table S4 below) used to infer the wavelength, amplitude, and rate of range of dynamic topography. For details see section below. A. Amplitude of the dynamic topography across the box domain. The solid red circle indicates the time and amplitude of the instant of time shown in panels B-D. B. Dynamic topography across the box. The scaled dimension across the box is 1,000 km. C. Temperature field. D. Effective viscosity for the non-linear viscosity, influenced by both temperature and strain rate. Scaled values obtained found using parameters in Table S2.

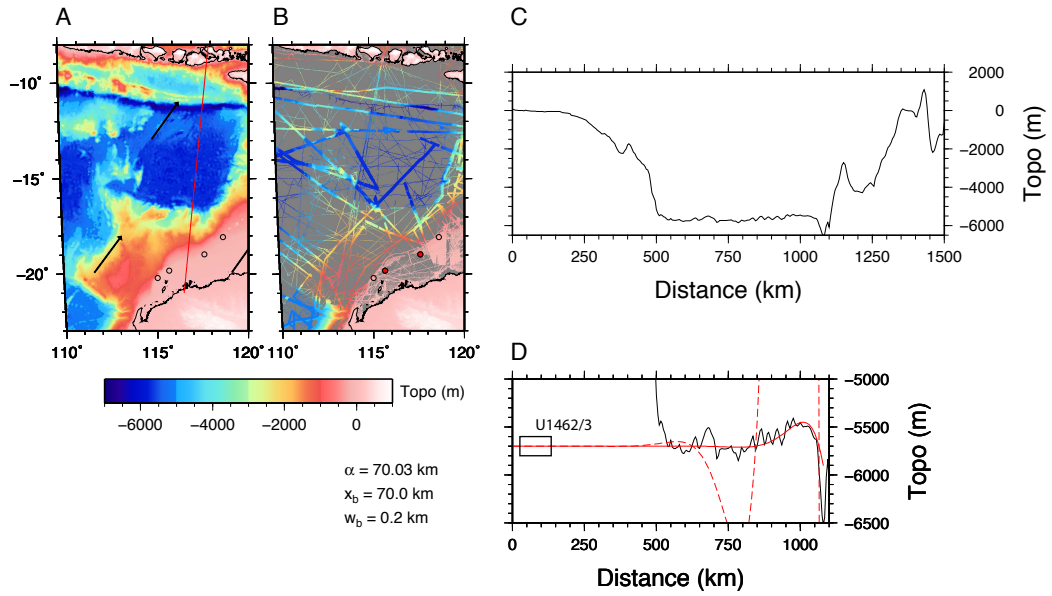

Figure S11. Interpolated topography (Smith and Sandwell, 1997) (A) and actual topography as ship-based measurements (B). C. Profile along the track shown in A (red line) from the drill sites of interest to the Timor Trench. D. Topography in the vicinity of the Timor Trench fit with a universal plate flexural model. The best fitting profile is shown as the solid red line and has a flexural parameter, α, of 70 km (with a mantle density ρ_m=3,300 kg m-3) this implies a plate rigidity of 10^{21} N-m. The best fitting model increased by 10X shown as the dashed red line. Position of Sites U1462 and U1463 with respect to the trench shown as the solid black rectangle.

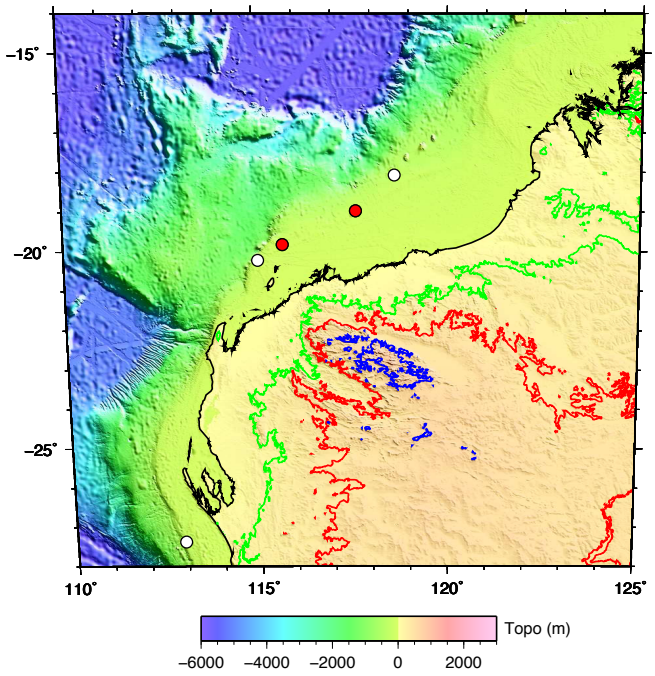

Figure S12. Topography of Australia with elevation contours at 200 m (green), 400 m (red) and 700 m (blue).

Mantle Flow Models

We consider the degree to which mantle flow fits the patterns of topography inferred from the kinematic models described in the main text. Two different kinds of models are considered, those in which the anomalies are detached from the lithosphere and those in which anomalies, due to their higher viscosity, are attached to the base of the lithosphere. See the Next Section in the Supplement for computational details.

An approximately 300 meter, 400 km wide topographic depression can be created with a cylindrical load generating viscous flow below the lithosphere (Fig. 6A, IF01, heavy solid line); this mantle anomaly has a diameter of about 80 km across with a temperature perturbation of 350^{o}C (or about 40 kg/m^{3}) while being 200 km below the surface, but only about 50 km below the lithosphere (Fig. S8). This flow model is roughly consistent with the maximum subsidence found in the kinematic model (Fig. 5B). With diffusion creep within the upper mantle, there is an approximately linear relation between topographic amplitude and the magnitude of the temperature (or density) anomaly. It is not possible to make the width of this anomaly much narrower than this, while still having the load detached from the lithosphere. A smaller diameter cylinder with a larger temperature difference results in nearly the same width (Fig. 6A, IF04, thin black line). Essentially, smaller loads, with the same integrated buoyancy, continue to generate surface perturbations proportional to their depth (Parsons and Daly, 1983); point loads excite flow at both long and short wavelengths, but the short wavelengths decay more quickly, such that a prominent signal proportional to the depth of the load remains. The load could be made shallower in order to decrease the wavelength of the dynamic topography, but that would require an unrealistically thin lithosphere. Eventually, shallower loads mechanically merge with the lithosphere.

Anomalies mechanically fixed to the lithosphere can also fit the instantaneous topography. For example, a low temperature anomaly that is about 120 km across with a perturbation of 280^{o}C (or about 30 kg/m^{3}) fully embedded into the base of the lithosphere (Fig. S9) can give such a depression (Fig. 6B, heavy black line). Anomalies fixed to the lithosphere are wider but have lower temperature anomalies compared to detached anomalies in the mantle (Table S3). A variety of combinations of anomaly widths (as long as they are on the order of the width of the surface depression), depth distributions, and amplitudes can be found which could match such an instantaneous depression. There is an approximate linear trade-off between temperature anomaly and topography and between the depth extent and the topography, as long as the length is less than the depth of the upper mantle (Moresi and Gurnis, 1996). However, if such an anomaly can simultaneously match subsidence rates require full convection models, which are described next.

Computational Methods for Models of Mantle Flow & Small-Scale Convection.

We computed small scale convection at the base of a thermal lithosphere using a formulation of a viscous fluid with a temperature- and stress-dependent viscosity. We used the Underworld2 software package[1] in which the numerical methods have been described by Moresi et al. (2003).

[1] Underworld 2 (http://www.underworldcode.org/) has doi: 10.5281/zenodo.1436039

Using the finite element method the Stokes and Energy equations are solved, as descried in Moresi et al. (2003). The problem is described by a Rayleigh number, defined as

$$Ra = \frac{\rho_o g \alpha_o h^3 \Delta T}{\eta_o \kappa}$$

Where the parameters are defined and nominal values given in Table S2. The non-dimensional aspect of a Cartesian box is 2x1 with 128 linear elements in the horizontal and 64 in the vertical. The model starts with a vertical thermal profile defined with the half-space cooling model with small thermal perturbations at the base of the thermal lithosphere. The temperature is non-dimensionalized by $T/\Delta T$ and the viscosity by η/η_o. Consequently, the non-dimensional viscosity, η', is described by:

$$\eta' = \eta'_o \dot{\epsilon}_{II}^{(1-n)/n} e^{\left[\frac{E'}{T'+T'_o} - \frac{E'}{1+T'_o}\right]}$$

Where E' is defined as $E'=E_a/(R\Delta T)$, where E_a is activation energy and R is the gas constant. There is an initial transient phase of convective overturn which is ignored in the subsequent spectral analysis of the surface topography. For the analysis of the topography we obtained amplitude specta for the topography amplitude and it's rate of change. For each wavelength we found those sets of values with the highest rates of change (which we referred to as subsidence rates). Those values are reported in the main text in Figure 7. We varied the ambient viscosity (pre-factor), activation energy, and a linear exponent for the mantle flow models (Table S3) and nonlinear exponent for the small-scale convection modes (Table S4). The IF models have loads attached to the lithosphere and characterized by an amplitude (A_o), a Gaussian width (s) and a depth (d). The AL models are cylinders detached from the lithosphere and characterized by an amplitude (A_o), a Gaussian radius (s) and a depth (d).

Table S2
Parameters for Small Scale Convection Models

Parameter		Value
g	Acceleration of gravity	10 m s^{-2}
h	Depth of domain	4.0 x 10^5 m
ρ_o	Reference density	4 x 10^3 kg m^{-3}
κ	Thermal diffusivity	10^{-6} m^2s^{-1}
η_o	Reference viscosity	1.0 x 10^{18} Pa s
α_v	thermal expansion	3.0 x 10^{-5} C^{-1}
ΔT	Temperature drop	1400 C
Ra	Rayleigh Number	1.075 x 10^8

Table S3
Summary of Mantle flow models

Run	n	A_o	s	d
AL01	1	0.2	0.15	0.25
AL02	1	0.23	0.15	0.25
AL03	1	0.2	0.15	0.35
AL04	1	0.2	0.05	0.25
Sink01	1	0.25	0.1	0.5
Sink02	1	0.3	0.1	0.5
Sink03	1	0.25	0.1	0.6
Sink04	1	1.0	0.05	0.5

Note: AL runs have anomalies attached to the lithosphere while Sink models have anomalies which are below the lithosphere. A_o is the non-dimensional maximum temperature perturbation, s is the non-dimensional Gaussian length-scale, and d is the non-dimensional depth of the anomaly (mid-point for Sink models and total depth extent for IF models). n is the stress-strain exponent in the viscosity law.

Table S4
Summary of Models of Small-Scale Convection

Run	Case	η_o(Pa)	Ra	τ_o (Myr)	E'	n	η'_o	A_o	Mode	Sample Time (Myr)	Notes
SSC12		10^{19}	$1.08x10^8$	200	35	3.0	10^2	0.25	SSCBL	180	
SSC13		10^{18}	$1.08x10^9$	125	35	3.0	10^2	0.005	SSCBL	5	
SSC14		10^{18}	$1.08x10^9$	125	35	3.0	10^2	0.25	SSCBL	20	But initial pert remains
SSC15		10^{18}	$1.08x10^9$	125	35	3.0	10^3	0.25	PLD		
SSC16		10^{18}	$1.08x10^9$	125	45	3.25	10^3	0.25	LO/PLD		
SSC17		10^{18}	$1.08x10^9$	125	45	2.75	10^3	0.25	LO		
SSC18		10^{18}	$1.08x10^9$	125	35	3.0	$2x10^2$	0.005	SSCBL	12	
SSC19		10^{18}	$1.08x10^9$	125	30	3.0	$2x10^2$	0.005	SSCBL	12	
SSC20		10^{18}	$1.08x10^9$	100	45	3.0	$2x10^2$	0.005	SSCBL	20	
SSC21		10^{18}	$1.08x10^9$	125	45	3.5	$2x10^2$	0.005	SSCBL	15	
SSC22		5×10^{18}	$2.15x10^8$	125	35	3.0	10	0.005	SSCBL	27	
SSC23		5×10^{17}	$2.15x10^8$	125	35	3.0	5×10^2	0.005	SSCBL	20	

Mode: SSCBL (Small scale convection below lithosphere); LO (lithosphere overturn); PLD (permanent lithosphere deformation).

References

BOC, 1972. Picard No. 1 Well Completion Report. BOC of Australia Ltd., p. 190.

Buckley, T., 2016. Cenozoic Stratigraphy of the North Perth Basin and the formation of the Houtman Abrolhos. University of Melbourne, Melbourne, Australia, p. 190.

Burt, A.J., 2003. Morangie 1 & 1st1 Well Completion Report. Origin Energy Developments Pty Ltd., p. 360.

Galloway, 1978. Well Completion Report, Houtman-1. Esso Australia Ltd., p. 213.

Moresi, L.N., Dufour, F., Mühlhaus, H.-B., 2003. A Lagrangian integration point finite element method for large deformation modeling of viscoelastic geomaterials. J. Comp. Phys 184, 476-497.

Moresi, L.N., Gurnis, M., 1996. Constraints on the lateral strength of slabs from three-dimensional dynamic flow models. Earth Planet. Sci. Lett. 138, 15-28.

Parsons, B., Daly, S., 1983. The Relationship Between Surface Topography, Gravity Anomalies, and Temperature Structure of Convection. J. Geophys. Res. 88, 1129-1144.

Seton, M., Müller, R.D., Zahirovic, S., Gaina, C., Torsvik, T., Shephard, G., Talsma, A., Gurnis, M., Turner, M., Maus, S., Chandler, M., 2012. Global continental and ocean basin reconstructions since 200 Ma. Earth Science Reviews 113, 212-270.

Smith, W.H.F., Sandwell, D.T., 1997. Global sea floor topography from satellite altimetry and ship depth soundings. Science 277, 1956-1962.

Woodside, 1982. Fisher No1 Well Completion Report. Woodside Offshore Pet. Pty. Ltd., p. 350.

Young, R.J.B., Wright, J.C., 1975. Carnarvon Basin West Tryal Rocks No. 2 Well Completion Report West Australian Petroleum Pty. Ltd., p. 296.